Engineering Analysis with Boundary Elements 113 (2020) 219–231

Contents lists available at ScienceDirect

Engineering Analysis with Boundary Elements

journal homepage: www.elsevier.com/locate/enganabound

A dual interpolation boundary face method for exterior acoustic problems based on the Burton–Miller formulation

Jianming Zhang*, Weicheng Lin, Xiaomin Shu, Yudong Zhong

State Key Laboratory of Advanced Design and Manufacturing for Vehicle Body, College of Mechanical and Vehicle Engineering, Hunan University, Changsha 410082, China

ARTICLE INFO

Keywords:
Acoustic problems
Dual interpolation boundary face method
Boundary face method
Moving least-squares approximation
Burton–Miller formulation

ABSTRACT

A dual interpolation boundary face method (DiBFM) based on the Burton–Miller formulation for solving exterior acoustic problems is presented. The method is able to unify the conforming and nonconforming BFM. In DiBFM implementation, the nodes of a conforming element are divided into two categories: source nodes (inside the element) and virtual nodes (on the boundary of the element). Acoustic pressure and its derivative are approximated using conforming elements, in the same way as conforming BFM. However, the Burton–Miller integral equations are just collocated at source nodes, in the same way as nonconforming BFM. To arrive at a square linear system, additional constraint equations established by the moving least-squares approximation are provided to condense the degrees of freedom relating to virtual nodes. Several numerical examples demonstrate the accuracy and efficiency of the proposed method.

1. Introduction

Solving acoustic problems is one of the most important applications of boundary face method (BFM) [1], boundary element method (BEM) [2–6] and finite element method (FEM) [7]. It can be used for predicting sound fields for noise control in submarines, airplanes, automobiles and many other consumer products. As is well known, BEM is a popular numerical technique for finding solutions to the exterior acoustic wave problems, because Sommerfeld radiation condition at infinity is able to be satisfied automatically. It is also popular due to its unique advantages in discretizing the boundary of the structure only and using the nonconforming elements. This makes the mesh generation a simpler process. Like BEM, BFM [8–11] is also based on a boundary integral equation (BIE), but by using Computer Aided Design (CAD) geometries directly no geometric error will be introduced.

The early research work of the BEM for acoustic problems has been performed by Banaugh and Goldsmith [12], and Copley [13], which can be traced back to the 1960s. In the work, a solution method based on the conventional boundary integral equation (CBIE) has been presented. For the exterior acoustic problems, however, the method results in a non-unique solution at the eigen-frequencies for the corresponding interior problem. This is a purely mathematical phenomenon. Two common methods of overcoming this phenomenon are the Combined Helmholtz Integral Equation Formulation (CHIEF) method and the Burton–Miller method.

The CHIEF method [14], proposed by Schenck, constructs some additional Helmholtz integral equations at interior nodes of the structure, which are added in the original system of linear algebraic equations. The main difficulty of this method, however, is how to properly choose the number and location of interior nodes. To this end, Wu and Seybert [15], and Juhl [16] have further developed the CHIEF method to ensure a unique solution. Chen et al. [17] have presented a rigorous analytical and numerical investigation of this method.

The Burton–Miller method [18], proposed by Burton and Miller, employs a complex linear combination of the CBIE and hypersingular boundary integral equation (HBIE). This method has been widely used by many others in their research on the BEM for exterior acoustic problems [1,2,4]. The major difficulty of this method is the evaluation of the hypersingular integral. To this end, various hypersingular integral techniques have been developed [19,20]. For example, Liu [21] proposed the weakly singular form of the HBIE; Guiggiani [22] presented a general algorithm which regularizes hypersingular integrals based on expanding the singular kernel at singular points by using Taylor series; Gao [23] proposed an efficient approach for evaluating boundary integrals with arbitrarily high-order singularities.

In conventional BFM and BEM implementation, the nonconforming and conforming elements have their own advantages and disadvantages [24–26]. Nonconforming element (see Fig. 1(a)) possesses some attractive advantages. For example, it is able to simplify the evaluation of the hypersingular integrals in Burton–Miller integral equation and greatly

* Corresponding author.
E-mail address: zhangjm@hnu.edu.cn (J. Zhang).

https://doi.org/10.1016/j.enganabound.2020.01.005
Received 20 January 2019; Received in revised form 24 October 2019; Accepted 9 January 2020
Available online 24 January 2020

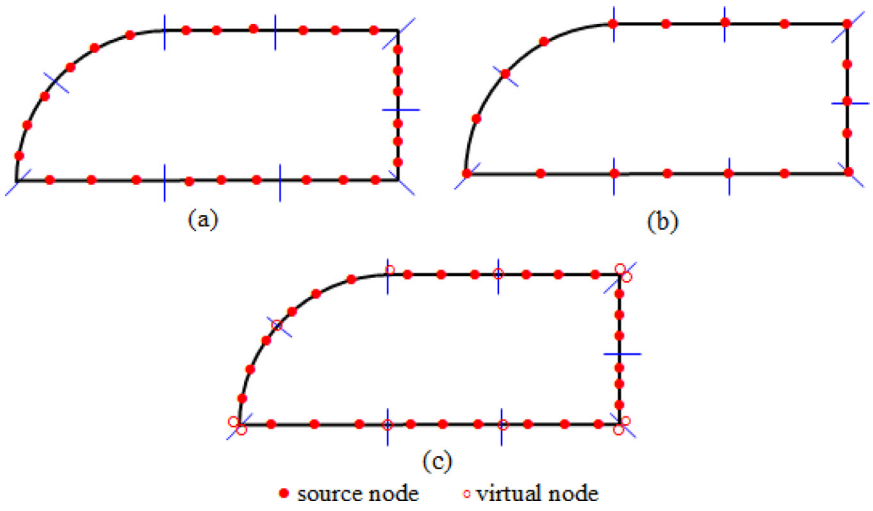

Fig. 1. Boundary discretized by quadratic elements: (a) nonconforming elements, (b) conforming elements, and (c) dual interpolation elements.

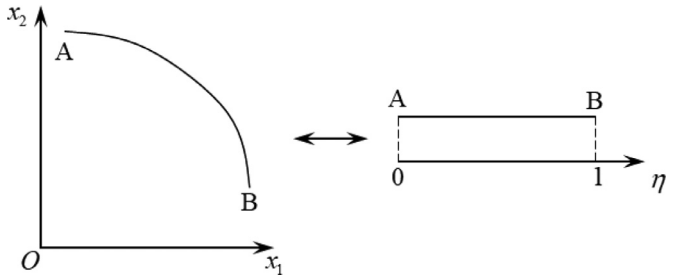

Fig. 2. Mapping between the Euclidean space and the parametric space of a curve.

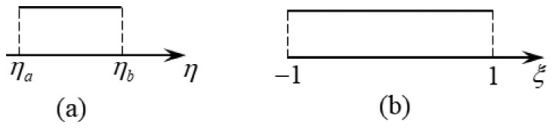

Fig. 3. Boundary element: (a) in parametric space of a curve, and (b) in space of intrinsic coordinates.

alleviating the task of mesh generation. For the same level of interpolation accuracy, however, it needs much more source nodes than conforming element. Conforming element (see Fig. 1(b)) can ensure the C° continuity, but not ensure the $C^{1,\alpha}$ continuity for source nodes at interfaces between elements, which is necessary for the evaluation of the hypersingular integrals [22]. It is inconvenient and inaccurate when used to approximate discontinuous fields, such as the normal derivative of the acoustic pressure at corners and edges of a scatterer. In addition, the solution's convergence rate is the same using either conforming or nonconforming elements, only depending on the degree of the polynomial used to approximate physical variables [26].

To unify the conforming and nonconforming elements in BFM and BEM implementation, Zhang proposed the dual interpolation boundary face method (DiBFM) [27–30]. In the DiBFM, an element is composed of a combination of source and virtual nodes, and that is called dual interpolation element (see Fig. 1(c)). The interpolation accuracy of the new elements is increased by two orders, compared with the corresponding conventional nonconforming elements. In addition, the method has an ability to readily and accurately approximate both continuous and discontinuous fields.

In this paper, we first combine the DiBFM with the Burton–Miller formulation to solve two- dimensional (2D) exterior acoustic wave problems. In our implementation, acoustic pressure and its derivative are approximated using the dual interpolation elements (first-layer interpolation), in the same way as conforming BFM. But the Burton–Miller integral equations are collocated only at source nodes, in the same way as nonconforming BFM. That is to say, the number of unknown quantities is more than the number of linear equations after the discretization of the Burton–Miller integral equation. In order to arrive at a square linear system, additional constraint equations are needed to condense the degrees of freedom relating to virtual nodes. These constraint equations are established using the moving least-squares (MLS) approximation (second-layer interpolation).

This paper is organized as follows. In Section 2, the parameter mapping scheme is described. In Section 3, the dual interpolation method is briefly presented. Section 4 describes a general formulation of the DiBFM for acoustic problem based on the Burton–Miller formulation. A number of numerical examples are given in Section 5. The paper ends with conclusions and discussions in Section 6.

2. Parameter mapping scheme

In 2D DiBFM, both dual interpolation and boundary integration are performed in parametric space of curves, which are exactly same as the B-rep data structure in most CAD software.

A parametric form of a curve can be expressed as:

$$\begin{cases} x_1 = x_1(\eta) \\ x_2 = x_2(\eta) \end{cases}, \qquad \eta \in [0,1], \tag{1}$$

where η is the parametric coordinate defined on a curve (see Fig. 2), and η is calculated by the following transformation:

$$\eta = 0.5(\eta_b + \eta_a) + 0.5(\eta_b - \eta_a)\xi, \qquad \xi \in [-1,1], \tag{2}$$

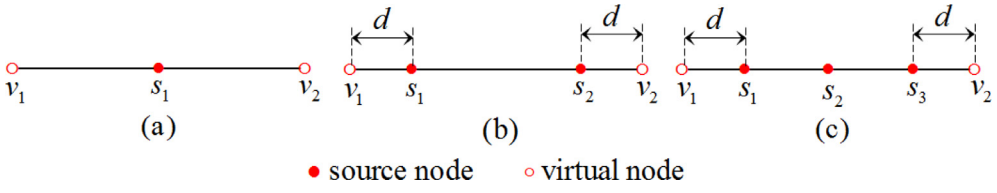

Fig. 4. Dual interpolation elements in 2D problems: (a) S1, (b) S2, and (c) S3.

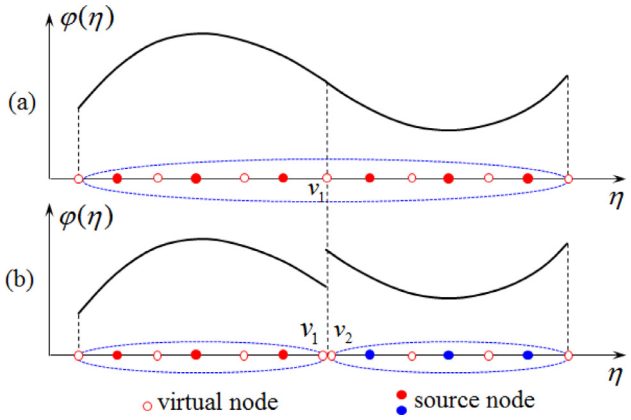

Fig. 5. Influence domains of virtual node: (a) for approximating continuous field, and (b) for approximating discontinuous field.

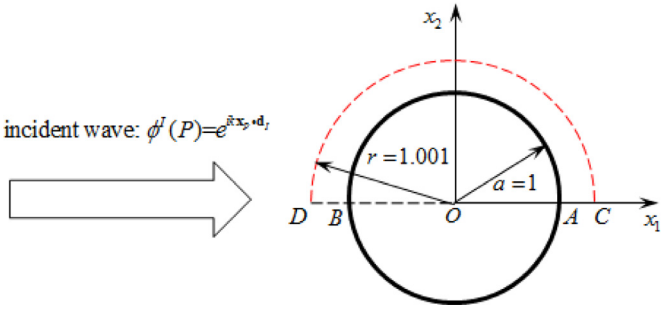

Fig. 6. Scattering from an infinite rigid cylinder with radius $a = 1$.

where ξ is the intrinsic coordinate defined on a boundary element (see Fig. 3). In this scheme, the geometric data (e.g. coordinates, outward normal, tangent vector and Jacobian) are evaluated from curves directly rather than from elements. Obviously, no geometric errors are introduced even in a coarse mesh.

3. Dual interpolation method

3.1. Dual interpolation element

In the DiBFM, the elements are called dual interpolation elements. The nodes of the new elements are divided into two categories: source and virtual nodes (see Fig. 4). Ignoring virtual nodes, they become conventional nonconforming elements (see Fig. 1(a)). When both the source and virtual nodes are taken into account, they are equivalent to standard conforming elements (see Fig. 1(b)). In this way, the dual interpolation

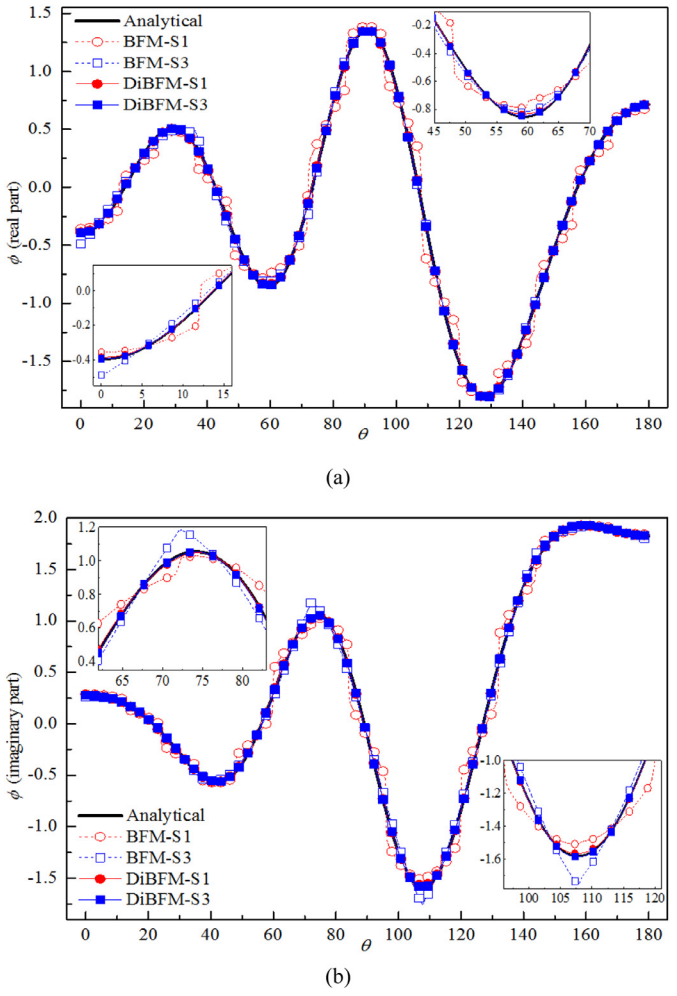

Fig. 8. Acoustic pressure along the curve *CD*, for the rigid cylinder scattering problem, for $ka = 5$: (a) real part and (b) imaginary part.

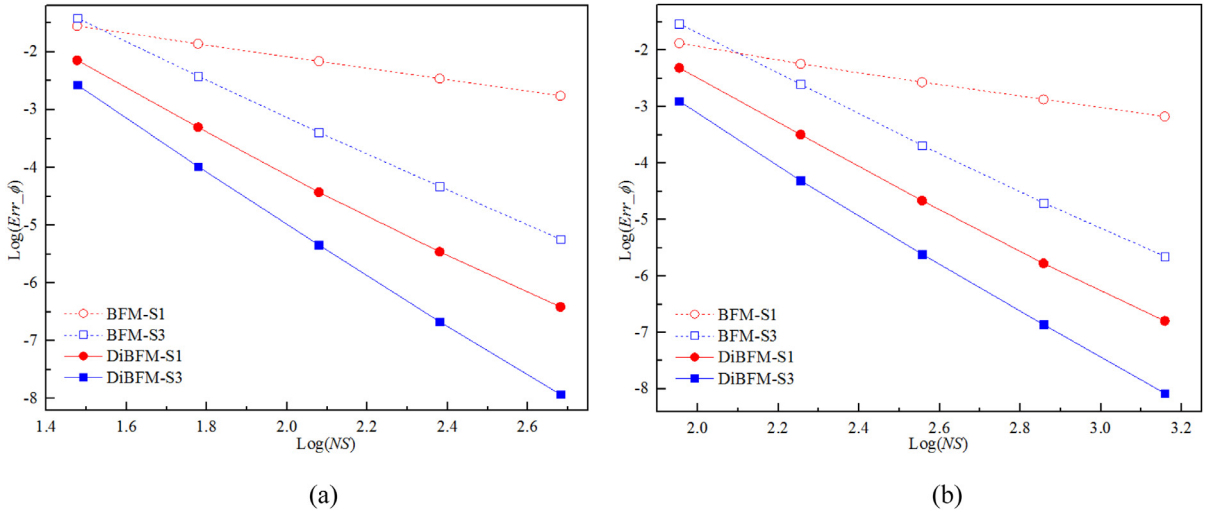

Fig. 7. Comparison of accuracy of DiBFM and BFM for the rigid cylinder scattering problem: (a) $ka = 5$ and (b) $ka = 15$.

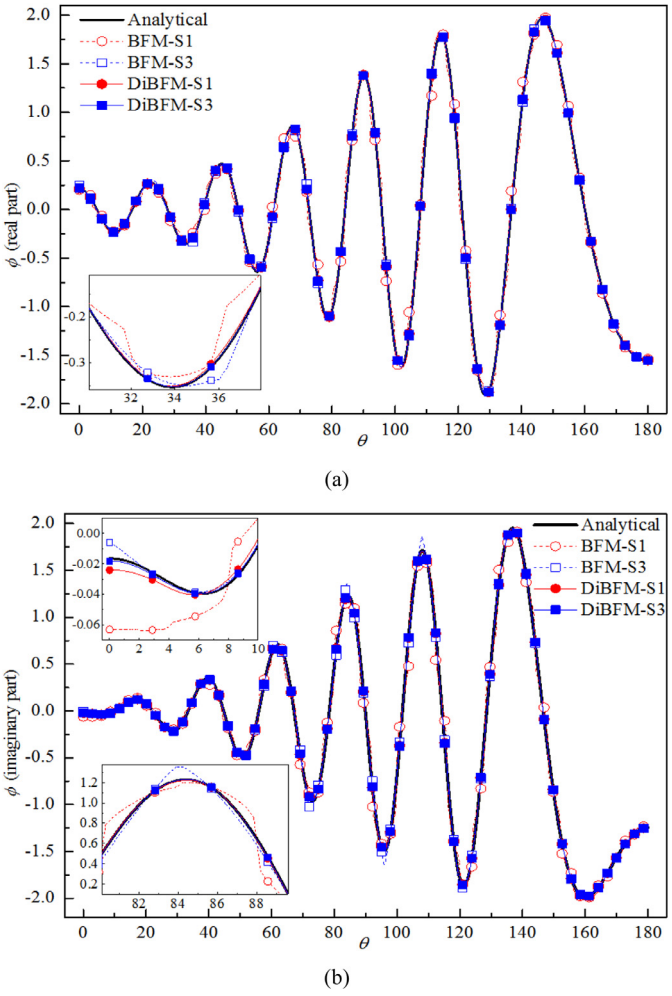

Fig. 9. Acoustic pressure along the curve *CD*, for the rigid cylinder scattering problem, for $ka = 15$: (a) real part and (b) imaginary part.

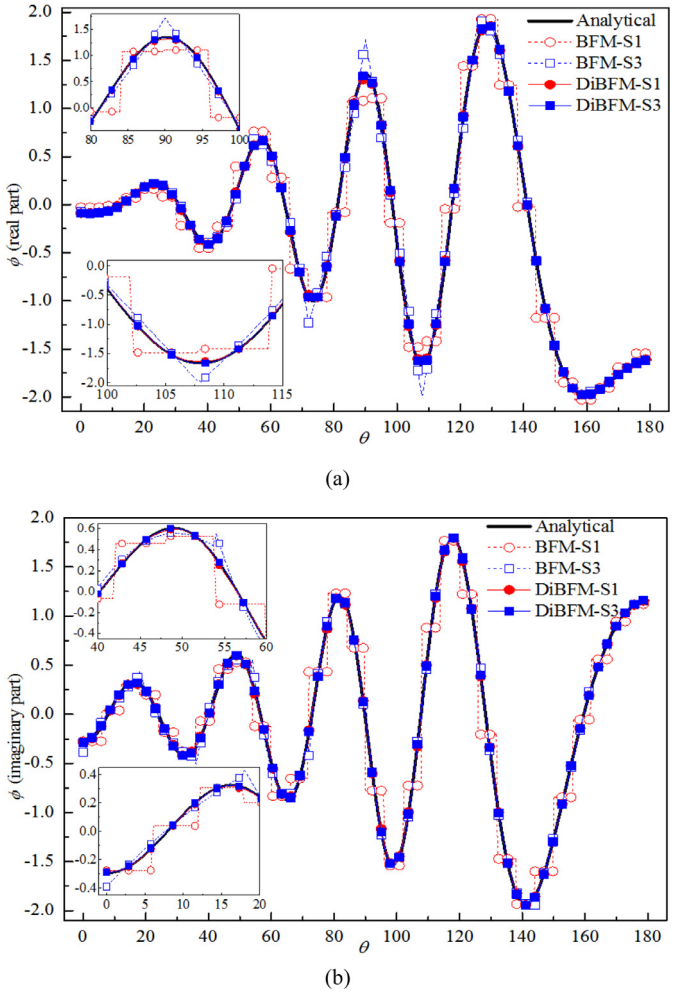

Fig. 10. Acoustic pressure along the curve *AB*, for the rigid cylinder scattering problem, for $ka = 10$: (a) real part and (b) imaginary part.

elements have an ability to unify the conforming and nonconforming elements.

As shown in the Figure, we identify the new elements with the notation S1, S2, S3 indicating the number of source nodes. The notation comes from the fact that in DiBFM the degrees of freedom associated with the virtual nodes are condensed and hence they do not appear in the final linear system to be solved. Shape functions of the S1, S2 and S3 elements are Eqs. (3), (4) and (5), respectively.

$$N_1^s(\xi) = (1-\xi)(1+\xi) \text{ and } \begin{cases} N_1^v(\xi) = 0.5\xi(\xi-1) \\ N_2^v(\xi) = 0.5\xi(\xi+1) \end{cases}, \tag{3}$$

$$\begin{cases} N_1^s(\xi) = \frac{[\xi-(1-d)](\xi+1)(\xi-1)}{2d(1-d)(2-d)} \\ N_2^s(\xi) = -\frac{[\xi+(1-d)](\xi+1)(\xi-1)}{2d(1-d)(2-d)} \end{cases} \text{ and } \begin{cases} N_1^v(\xi) = -\frac{[\xi+(1-d)][\xi-(1-d)](\xi-1)}{2d(2-d)} \\ N_2^v(\xi) = \frac{[\xi+(1-d)][\xi-(1-d)](\xi+1)}{2d(2-d)} \end{cases}, \tag{4}$$

$$\begin{cases} N_1^s(\xi) = -\frac{[\xi-(1-d)](\xi+1)(\xi-1)\xi}{2d(2-d)(1-d)^2} \\ N_2^s(\xi) = \frac{[\xi+(1-d)][\xi-(1-d)](\xi+1)(\xi-1)}{(1-d)^2} \\ N_3^s(\xi) = -\frac{[\xi+(1-d)](\xi+1)(\xi-1)\xi}{2d(2-d)(1-d)^2} \end{cases} \text{ and } \begin{cases} N_1^v(\xi) = \frac{[\xi+(1-d)][\xi-(1-d)](\xi-1)\xi}{2d(2-d)} \\ N_2^v(\xi) = \frac{[\xi+(1-d)][\xi-(1-d)](\xi+1)\xi}{2d(2-d)} \end{cases}, \tag{5}$$

where d is the offset of source nodes, which is taken to be 0.25 in this paper.

It should be noted that the interpolation in the dual interpolation elements is increased by two orders, in comparison with the order of interpolation function of the corresponding nonconforming elements using the source nodes alone. This leads to a considerable improvement in accuracy.

3.2. First-layer interpolation

The first-layer interpolation is similar to the interpolation in a standard conforming element. The difference is that the shape functions in the present method relating to both source and virtual nodes are used. For an arbitrary quantity u, the first-layer interpolation form is:

$$u(x_1, x_2) = u(\eta) = u(\xi) = \sum_{\alpha=1}^{n\alpha} N_\alpha^s(\xi) u(Q_\alpha^s) + \sum_{\kappa=1}^{n\kappa} N_\kappa^v(\xi) u(Q_\kappa^v), \tag{6}$$

where $n\alpha$ and $n\kappa$ are the total number of source and virtual nodes belonging to the dual interpolation element, respectively. $N_\alpha^s(\xi)$ and $u(Q_\alpha^s)$ are the shape function and nodal value of the α^{th} source node, respectively. $N_\kappa^v(\xi)$ and $u(Q_\kappa^v)$ are the shape function and nodal value of the κ^{th} virtual node, respectively. In DiBFM, $u(Q_\kappa^v)$ is not an independent variable, and it is determined by the second-layer interpolation.

3.3. Second-layer interpolation

The second-layer interpolation has an ability to readily and accurately approximate both continuous and discontinuous fields. In DiBFM implementation, it is just used to establish the relationships between source and virtual nodes, rather than evaluate the shape functions at each Gauss point in the numerical integration process. The degrees of

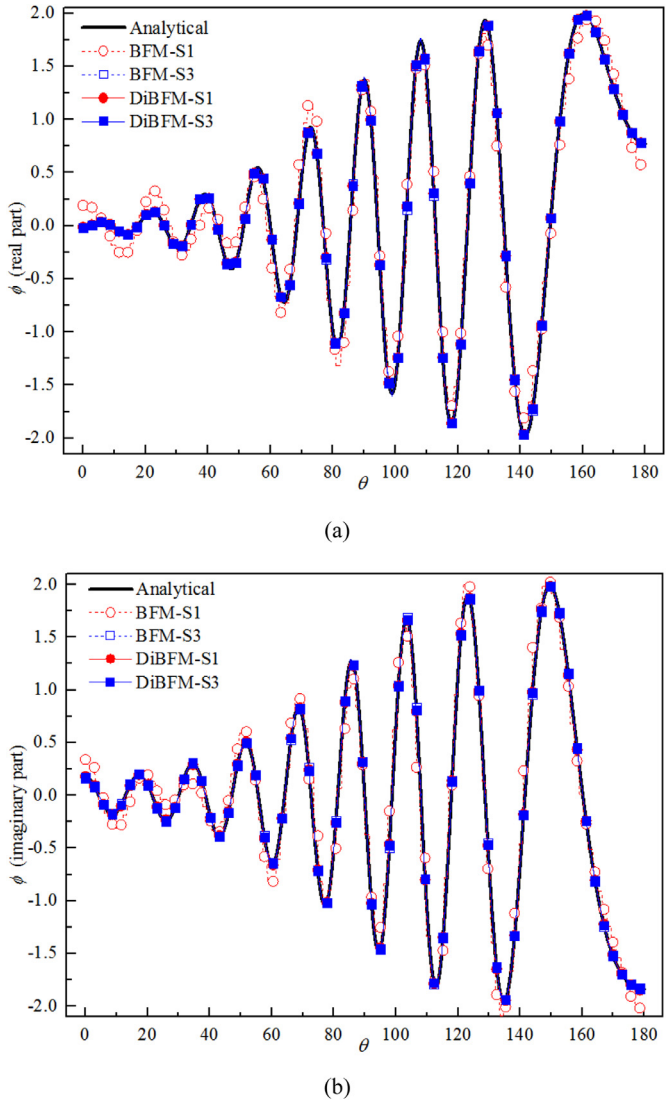

Fig. 11. Acoustic pressure along the curve *AB*, for the rigid cylinder scattering problem, for $ka = 20$: (a) real part and (b) imaginary part.

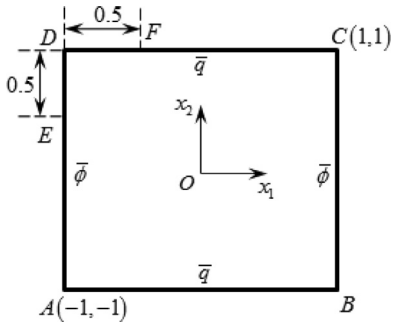

Fig. 13. Radiation from a square.

freedom relating to virtual nodes are condensed by these relationships. This matter is addressed later in this paper.

In this paper, the second-layer interpolation is constructed by the MLS approximation. For the virtual nodal value $u(Q_\kappa^v)$, the second-layer interpolation form is:

$$u\left(Q_\kappa^v\right) = \sum_{m=1}^{m\kappa} \psi_m^{vs}\left(\eta_\kappa^v\right) u\left(Q_{m(\kappa)}^s\right), \tag{7}$$

where mk is the total number of source nodes $Q_{m(\kappa)}^s$ located in the influence domain of virtual node Q_κ^v, $u(Q_{m(\kappa)}^s)$ are the nodal value of source node $Q_{m(\kappa)}^s$, η_κ^v is the parametric coordinate of virtual node Q_κ^v, $\psi_m^{vs}(\eta_\kappa^v)$ is the second-layer interpolation shape function corresponding to source node $Q_{m(\kappa)}^s$:

$$\psi_m^{vs}\left(\eta_\kappa^v\right) = \sum_{n=1}^{m\kappa} \varphi_n^{vs}\left(\eta_\kappa^v\right)\left[\left(\boldsymbol{\varphi}^{ss}\right)^{-1}\right]_{nm}, \tag{8}$$

in which

$$\boldsymbol{\varphi}^{ss} = \left[\varphi_n^{ss}\left(\eta_{m(\kappa)}^s\right)\right],$$

where $\eta_{m(\kappa)}^s$ is the parametric coordinate of source node $Q_{m(\kappa)}^s$, $\varphi_n^{vs}(\eta_\kappa^v)$ and $\varphi_n^{ss}(\eta_m^s)$ are the MLS shape functions corresponding to source node $Q_{n(\kappa)}^s$. The details of the MLS approximation have been discussed in Ref. [31].

It should be noted that the dual interpolation method has an ability to readily and accurately approximate continuous and discontinuous fields, by manipulating the influence domains of some specific virtual nodes in the second-layer interpolation. To demonstrate the feature, an example is given in Fig. 5. For approximating a continuous field, we put

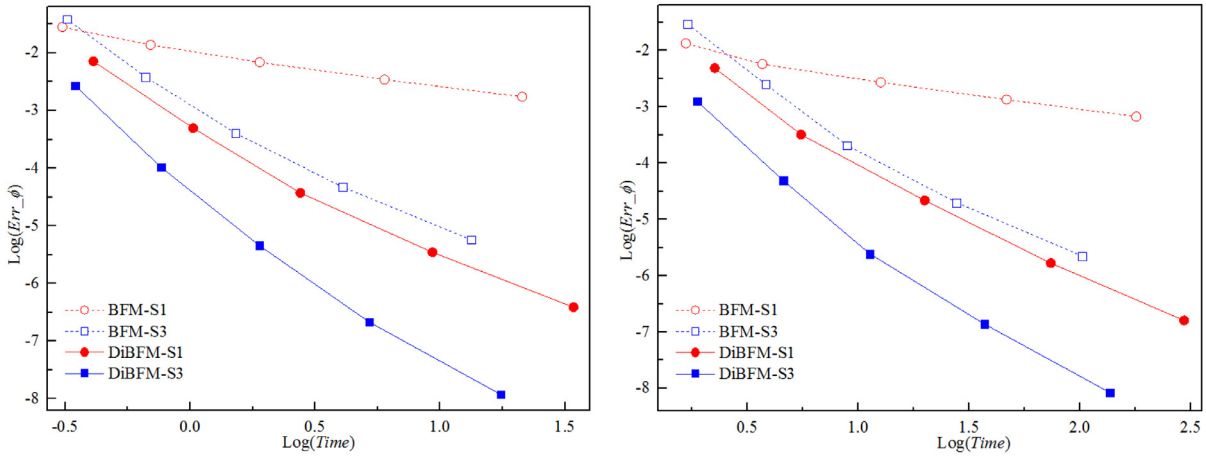

Fig. 12. Comparison of efficiency of DiBFM and BFM for the rigid cylinder scattering problem: (a) $ka = 5$ and (b) $ka = 15$.

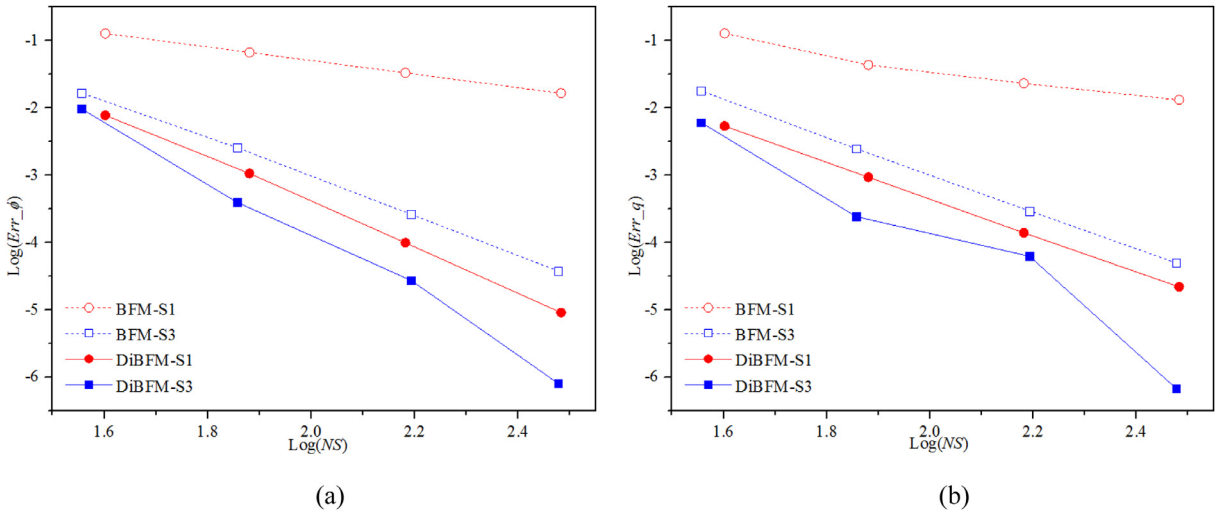

Fig. 14. Comparison of accuracy of DiBFM and BFM for the radiation problem: (a) ϕ on segment *DF* and (b) q on segment *ED*.

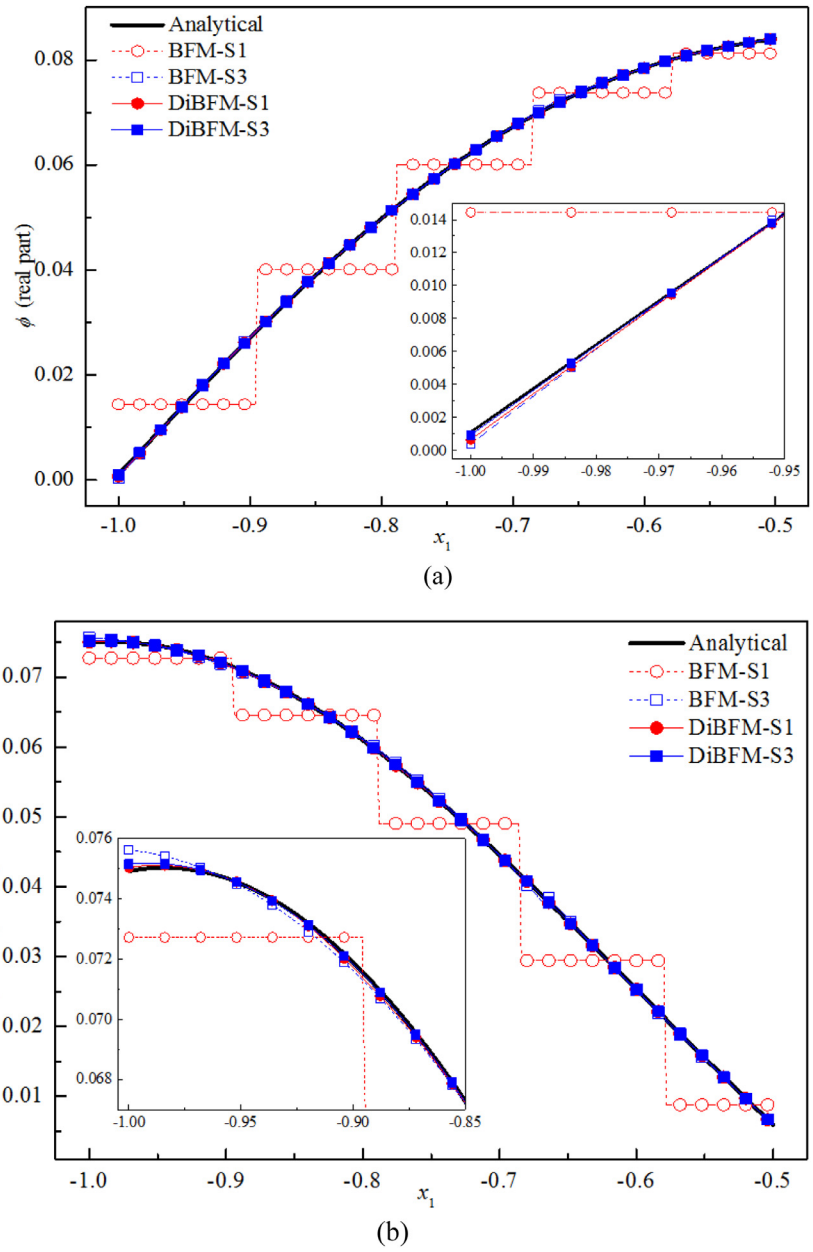

Fig. 15. Acoustic pressure along the segment *DF* for the radiation problem: (a) real part and (b) imaginary part.

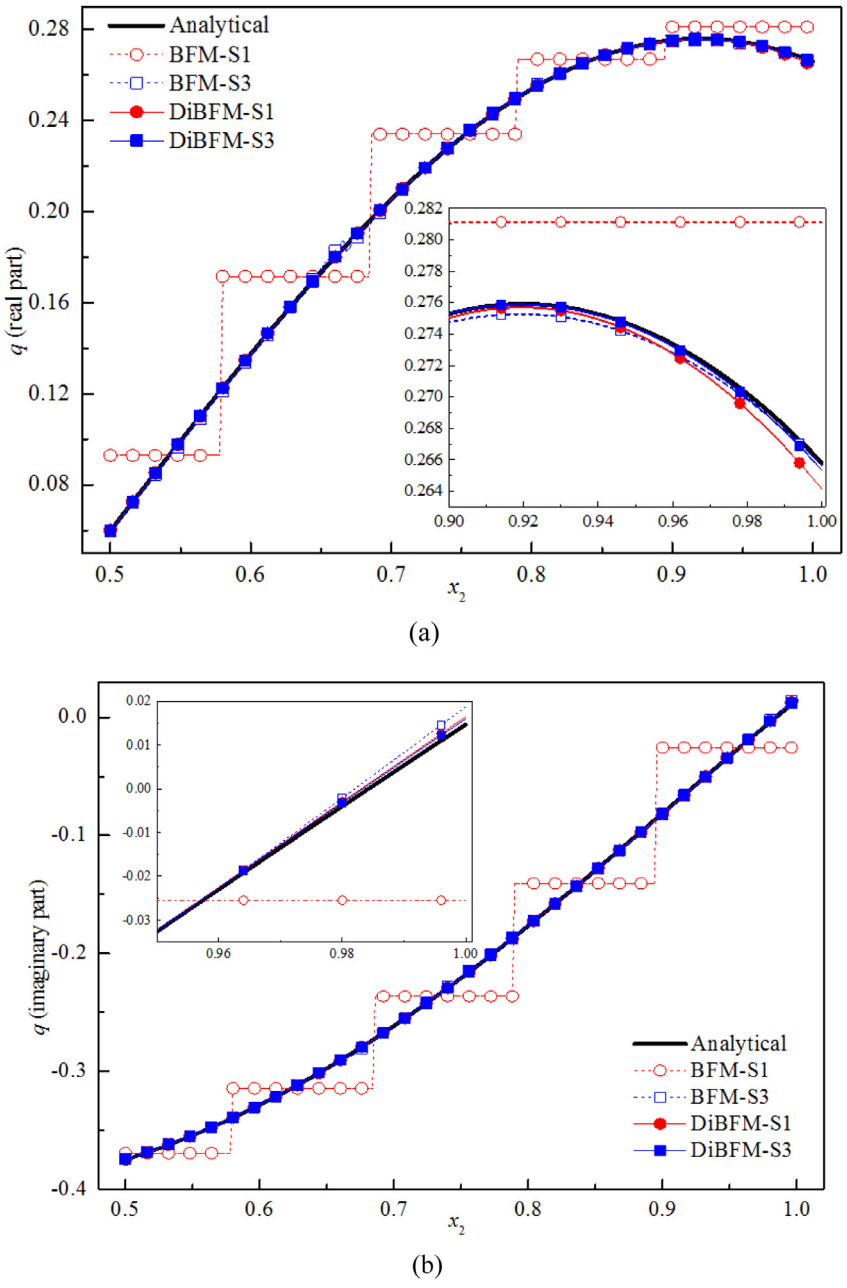

Fig. 16. Normal derivative of acoustic pressure along the segment *ED* for the radiation problem: (a) real part and (b) imaginary part.

only one virtual node v_1 at the element end point (see Fig. 5(a)), letting the two elements share a same virtual node, thus readily leading to continuity at the point. For modeling a discontinuous field, we put two virtual nodes (see Fig. 5(b)), one for each element. In this way, the three red source nodes in Fig. 5(b) located in the influence domain of virtual node v_1, while the three blue source nodes in Fig. 5(b) located in the influence domain of virtual node v_2. Obviously, the nodal values at the two nodes are different so that it is easier to model the discontinuous field.

4. DiBFM for acoustic problem based on the Burton–Miller formulation

4.1. Burton–Miller integral equation

Consider an acoustic problem in a 2D infinite domain Ω with boundary Γ. The Burton–Miller boundary integral equation for the problem is:

$$c(P)\phi(P)+\int_\Gamma \frac{\partial G(P,Q,k)}{\partial n(Q)}\phi(Q)d\Gamma(Q)+\beta\int_\Gamma \frac{\partial^2 G(P,Q,k)}{\partial n(Q)\partial n(P)}\phi(Q)d\Gamma(Q)$$
$$=\int_\Gamma G(P,Q,k)\frac{\partial\phi(Q)}{\partial n(Q)}d\Gamma(Q)+\beta\left[\int_\Gamma \frac{\partial G(P,Q,k)}{\partial n(P)}\frac{\partial\phi(Q)}{\partial n(Q)}d\Gamma(Q)-c(P)\frac{\partial\phi(P)}{\partial n(P)}\right],$$
$$+\phi^I(P)+\beta\frac{\partial\phi^I(P)}{\partial n(P)},\qquad P,Q\in\Gamma \tag{9}$$

in which

$$G(P,Q,k)=\frac{i}{4}H_0^{(1)}(kr),$$

where ϕ is the acoustic pressure, $\phi^I(P)$ is the incident acoustic wave (for scattering problems), k is the acoustic wavenumber, i is the imaginary unit, β is taken to be i/k, r is the distance between the field point Q and source node P, $n(Q)$ and $n(P)$ are the outward normal at field point Q and source node P, respectively. $H_0^{(1)}(\cdot)$ is the first-kind Hankel function of order zero. The coefficient $c(P)=1/2$ if Γ is smooth at source node P.

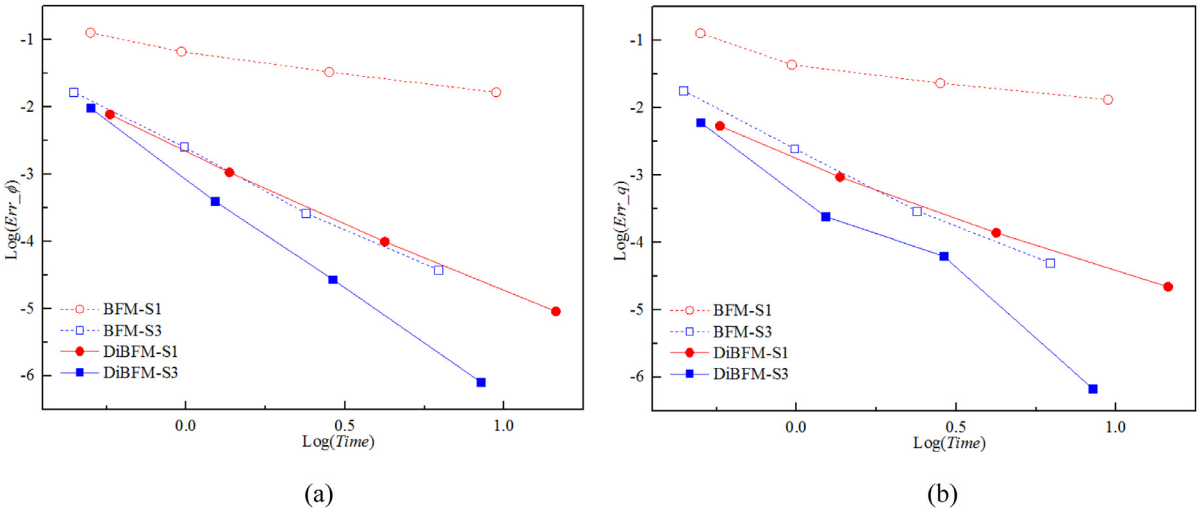

Fig. 17. Comparison of efficiency of DiBFM and BFM for the radiation problem: (a) ϕ on segment DF and (b) q on segment ED.

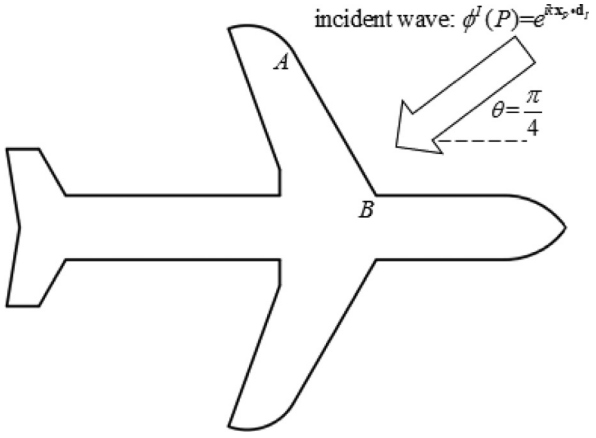

Fig. 18. Scattering from an airplane.

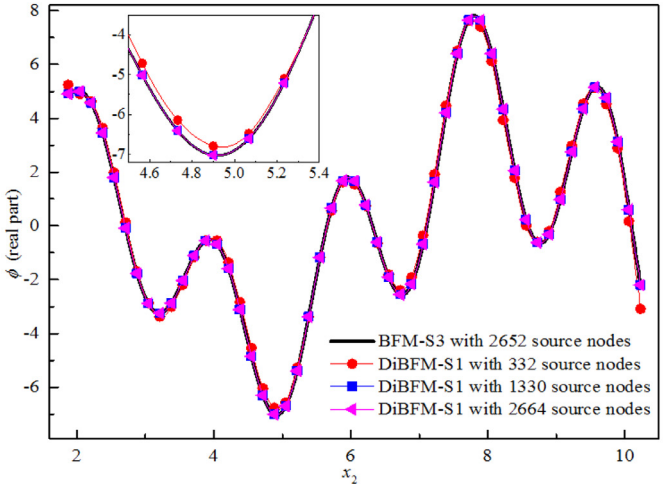

Fig. 19. Real part of acoustic pressure along the curve AB of the airplane scattering problem for $k = 3$: (a) DiBFM -S1 and (b) BFM-S1.

4.2. Discretization

In DiBFM implementation, the Burton–Miller integral equation, Eq. (9), is discretized by dual interpolation elements. However, only the source nodes are taken as collocation points in Eq. (9), and the source nodes are marked as P_l ($l = 1, 2, \ldots, NS$). The discretization form of Eq. (9) is:

$$\sum_{e=1}^{ne}\left[\sum_{\alpha=1}^{n\alpha} h^{ss}(P_l)\phi\left(Q^s_{e(\alpha)}\right)+\sum_{\kappa=1}^{n\kappa} h^{sv}(P_l)\phi\left(Q^v_{e(\kappa)}\right)\right]$$
$$=\sum_{e=1}^{ne}\left[\sum_{\alpha=1}^{n\alpha} g^{ss}(P_l)\frac{\partial\phi\left(Q^s_{e(\alpha)}\right)}{\partial n(Q)}+\sum_{\kappa=1}^{n\kappa} g^{sv}(P_l)\frac{\partial\phi\left(Q^v_{e(\kappa)}\right)}{\partial n(Q)}\right]+b^I(P_l), \tag{10}$$

in which

$$h^{ss}(P_l)=\int_{\Gamma_e}\frac{\partial G(P,Q,k)}{\partial n(Q)}N^s_{e(\alpha)}(Q)d\Gamma(Q)$$
$$+\beta\int_{\Gamma_e}\frac{\partial^2 G(P,Q,k)}{\partial n(Q)\partial n(P)}N^s_{e(\alpha)}(Q)d\Gamma(Q)+\frac{1}{2}\delta^k_{e(\alpha)},$$

$$h^{sv}(P_l)=\int_{\Gamma_e}\frac{\partial G(P,Q,k)}{\partial n(Q)}N^v_{e(\kappa)}(Q)d\Gamma(Q)$$
$$+\beta\int_{\Gamma_e}\frac{\partial^2 G(P,Q,k)}{\partial n(Q)\partial n(P)}N^v_{e(\kappa)}(Q)d\Gamma(Q),$$

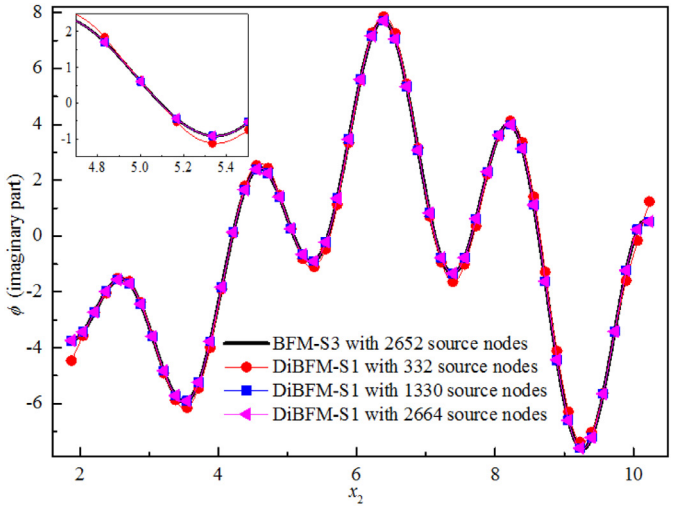

(a)

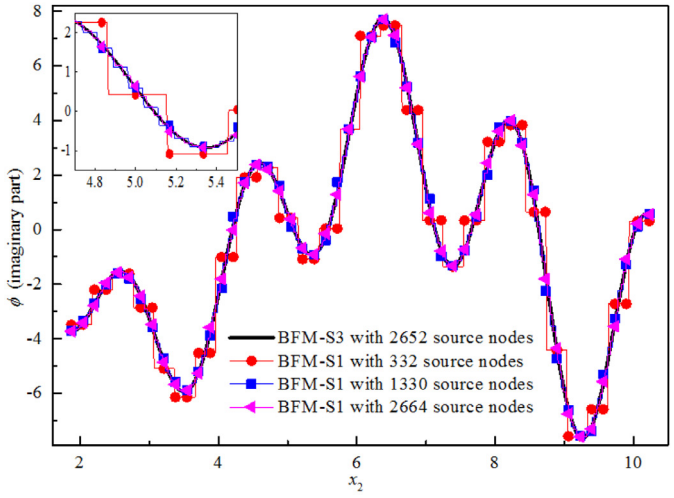

(b)

Fig. 20. Imaginary part of acoustic pressure along the curve *AB* of the airplane scattering problem for $k = 3$: (a) DiBFM -S1 and (b) BFM-S1.

$$g^{ss}(P_l) = \int_{\Gamma_e} G(P,Q,k) N^s_{e(\alpha)}(Q) d\Gamma(Q) + \beta \left[\int_{\Gamma_e} \frac{\partial G(P,Q,k)}{\partial n(P)} N^s_{e(\alpha)}(Q) d\Gamma(Q) - \frac{1}{2}\delta^k_{e(\alpha)} \right],$$

$$g^{sv}(P_l) = \int_{\Gamma_e} G(P,Q,k) N^v_{e(\kappa)}(Q) d\Gamma(Q) + \beta \int_{\Gamma_e} \frac{\partial G(P,Q,k)}{\partial n(P)} N^v_{e(\kappa)}(Q) d\Gamma(Q),$$

$$b^I(P_l) = \phi^I(P_l) + \beta \frac{\partial \phi^I(P_l)}{\partial n(P)},$$

and

$$\delta^k_{e(\alpha)} = \begin{cases} 1, & \text{if source node } P_k \text{ is the } \alpha^{\text{th}} \text{ source node in the } e^{\text{th}} \text{ element} \\ 0, & \end{cases}$$

where $N^s_{e(\alpha)}$ and $\phi(Q^s_{e(\alpha)})$ are the shape function and acoustic pressure of α^{th} source node in e^{th} dual interpolation element, respectively; $N^v_{e(\kappa)}$ and $\phi(Q^v_{e(\kappa)})$ are the shape function and acoustic pressure of κ^{th} virtual node on e^{th} dual interpolation element, respectively; Γ_e is the boundary of domain of e^{th} dual interpolation element.

The matrix form of Eq. (10) is:

$$\begin{bmatrix} \mathbf{H}^{ss}_{dd} & \mathbf{H}^{ss}_{dn} \\ \mathbf{H}^{ss}_{nd} & \mathbf{H}^{ss}_{nn} \end{bmatrix} \begin{Bmatrix} \bar{\mathbf{\Phi}}^s_d \\ \mathbf{\Phi}^s_n \end{Bmatrix} + \begin{bmatrix} \mathbf{H}^{sv}_{dd} & \mathbf{H}^{sv}_{dn} \\ \mathbf{H}^{sv}_{nd} & \mathbf{H}^{sv}_{nn} \end{bmatrix} \begin{Bmatrix} \bar{\mathbf{\Phi}}^v_d \\ \mathbf{\Phi}^v_n \end{Bmatrix} = \begin{bmatrix} \mathbf{G}^{ss}_{dd} & \mathbf{G}^{ss}_{dn} \\ \mathbf{G}^{ss}_{nd} & \mathbf{G}^{ss}_{nn} \end{bmatrix} \begin{Bmatrix} \mathbf{q}^s_d \\ \bar{\mathbf{q}}^s_n \end{Bmatrix} + \begin{bmatrix} \mathbf{G}^{sv}_{dd} & \mathbf{G}^{sv}_{dn} \\ \mathbf{G}^{sv}_{nd} & \mathbf{G}^{sv}_{nn} \end{bmatrix} \begin{Bmatrix} \mathbf{q}^v_d \\ \bar{\mathbf{q}}^v_n \end{Bmatrix} + \begin{Bmatrix} \mathbf{b}^I_d \\ \mathbf{b}^I_n \end{Bmatrix}, \tag{11}$$

where the subscripts *d* and *n* stand for the boundary conditions of Dirichlet and Neumann type, respectively.

4.3. Assembly and solution

Due to the fact that the Burton–Miller integral equations are collocated at source nodes only, the number of unknown quantities is more than the number of linear equations after the discretization of the BIE (see Eq. (11)). To make the final system of linear algebraic equations solvable, the degrees of freedom relating to virtual nodes in Eq. (11) need to be condensed using additional constraint equations. These equations are provided by the second-layer interpolation as below:

$$\mathbf{\Phi}^v_n = \begin{bmatrix} \mathbf{\Psi}^{vs}_{nd} & \mathbf{\Psi}^{vs}_{nn} \end{bmatrix} \begin{Bmatrix} \bar{\mathbf{\Phi}}^s_d \\ \mathbf{\Phi}^s_n \end{Bmatrix}, \tag{12}$$

$$\mathbf{q}^v_d = \mathbf{\Theta}^{vs}_{dd} \mathbf{q}^s_d, \tag{13}$$

where $\boldsymbol{\psi}^{vs}_{nd}$, $\boldsymbol{\psi}^{vs}_{nn}$ and $\mathbf{\Theta}^{vs}_{dd}$ are shape function matrices constructed by the second-layer interpolation. The derivation of the matrices is described in Section 3.3.

Substituting Eqs. (12) and (13) into Eq. (11) yields:

$$\begin{bmatrix} \bar{\mathbf{H}}^{ss}_{dd} & \bar{\mathbf{H}}^{ss}_{dn} \\ \bar{\mathbf{H}}^{ss}_{nd} & \bar{\mathbf{H}}^{ss}_{nn} \end{bmatrix} \begin{Bmatrix} \bar{\mathbf{\Phi}}^s_d \\ \mathbf{\Phi}^s_n \end{Bmatrix} + \begin{bmatrix} \mathbf{H}^{sv}_{dd} \\ \mathbf{H}^{sv}_{nd} \end{bmatrix} \bar{\mathbf{\Phi}}^v_d = \begin{bmatrix} \bar{\mathbf{G}}^{ss}_{dd} & \mathbf{G}^{ss}_{dn} \\ \bar{\mathbf{G}}^{ss}_{nd} & \mathbf{G}^{ss}_{nn} \end{bmatrix} \begin{Bmatrix} \mathbf{q}^s_d \\ \bar{\mathbf{q}}^s_n \end{Bmatrix} + \begin{bmatrix} \mathbf{G}^{sv}_{dn} \\ \mathbf{G}^{sv}_{nn} \end{bmatrix} \bar{\mathbf{q}}^v_n + \begin{Bmatrix} \mathbf{b}^I_d \\ \mathbf{b}^I_n \end{Bmatrix}, \tag{14}$$

in which

$$\begin{bmatrix} \bar{\mathbf{H}}^{ss}_{dd} & \bar{\mathbf{H}}^{ss}_{dn} \\ \bar{\mathbf{H}}^{ss}_{nd} & \bar{\mathbf{H}}^{ss}_{nn} \end{bmatrix} = \begin{bmatrix} \mathbf{H}^{ss}_{dd} & \mathbf{H}^{ss}_{dn} \\ \mathbf{H}^{ss}_{nd} & \mathbf{H}^{ss}_{nn} \end{bmatrix} + \begin{bmatrix} \mathbf{H}^{sv}_{dn} \\ \mathbf{H}^{sv}_{nn} \end{bmatrix} \begin{bmatrix} \mathbf{\Psi}^{vs}_{n_1 d_1} & \mathbf{\Psi}^{vs}_{n_1 n_1} \end{bmatrix},$$

$$\begin{bmatrix} \bar{\mathbf{G}}^{ss}_{dd} \\ \bar{\mathbf{G}}^{ss}_{nd} \end{bmatrix} = \begin{bmatrix} \mathbf{G}^{ss}_{dd} \\ \mathbf{G}^{ss}_{nd} \end{bmatrix} + \begin{bmatrix} \mathbf{G}^{sv}_{dd} \\ \mathbf{G}^{sv}_{nd} \end{bmatrix} \mathbf{\Theta}^{vs}_{dd},$$

By moving unknown quantities to the left-hand side and known quantities to the right-hand side in Eq. (14), a standard system of linear equations for acoustic problems is formed:

$$\mathbf{Ax=b}, \tag{15}$$

in which

$$\mathbf{A} = \begin{bmatrix} -\bar{\mathbf{G}}^{ss}_{dd} & \bar{\mathbf{H}}^{ss}_{dn} \\ -\bar{\mathbf{G}}^{ss}_{nd} & \bar{\mathbf{H}}^{ss}_{nn} \end{bmatrix},$$

$$\mathbf{x} = \begin{Bmatrix} \mathbf{q}^s_d & \mathbf{\Phi}^s_n \end{Bmatrix}^{\mathrm{T}},$$

$$\mathbf{b} = \begin{bmatrix} -\bar{\mathbf{H}}^{ss}_{dd} & \mathbf{G}^{ss}_{dn} \\ -\bar{\mathbf{H}}^{ss}_{nd} & \mathbf{G}^{ss}_{nn} \end{bmatrix} \begin{Bmatrix} \bar{\mathbf{\Phi}}^s_d \\ \bar{\mathbf{q}}^s_n \end{Bmatrix} + \begin{bmatrix} -\mathbf{H}^{sv}_{dd} & \mathbf{G}^{sv}_{dn} \\ -\mathbf{H}^{sv}_{nd} & \mathbf{G}^{sv}_{nn} \end{bmatrix} \begin{Bmatrix} \bar{\mathbf{\Phi}}^v_d \\ \bar{\mathbf{q}}^v_n \end{Bmatrix} + \begin{Bmatrix} \mathbf{b}^I_d \\ \mathbf{b}^I_n \end{Bmatrix},$$

where **A** is the coefficient matrix of dimensions $NS \times NS$ for 2D acoustic problems, and **b** is the known right-hand-side vector. **x** is the unknown vector only containing source nodes.

Since the unknown vector of the final system equations is including the source nodes only (see Eq. (15)), the size of the final linear system in our method is the same as that in the conventional BFM and BEM implementation. For the same number of source nodes, however, our method is able to possess much higher accuracy and improved convergence rates. This will be demonstrated by several numerical examples in Section 5.

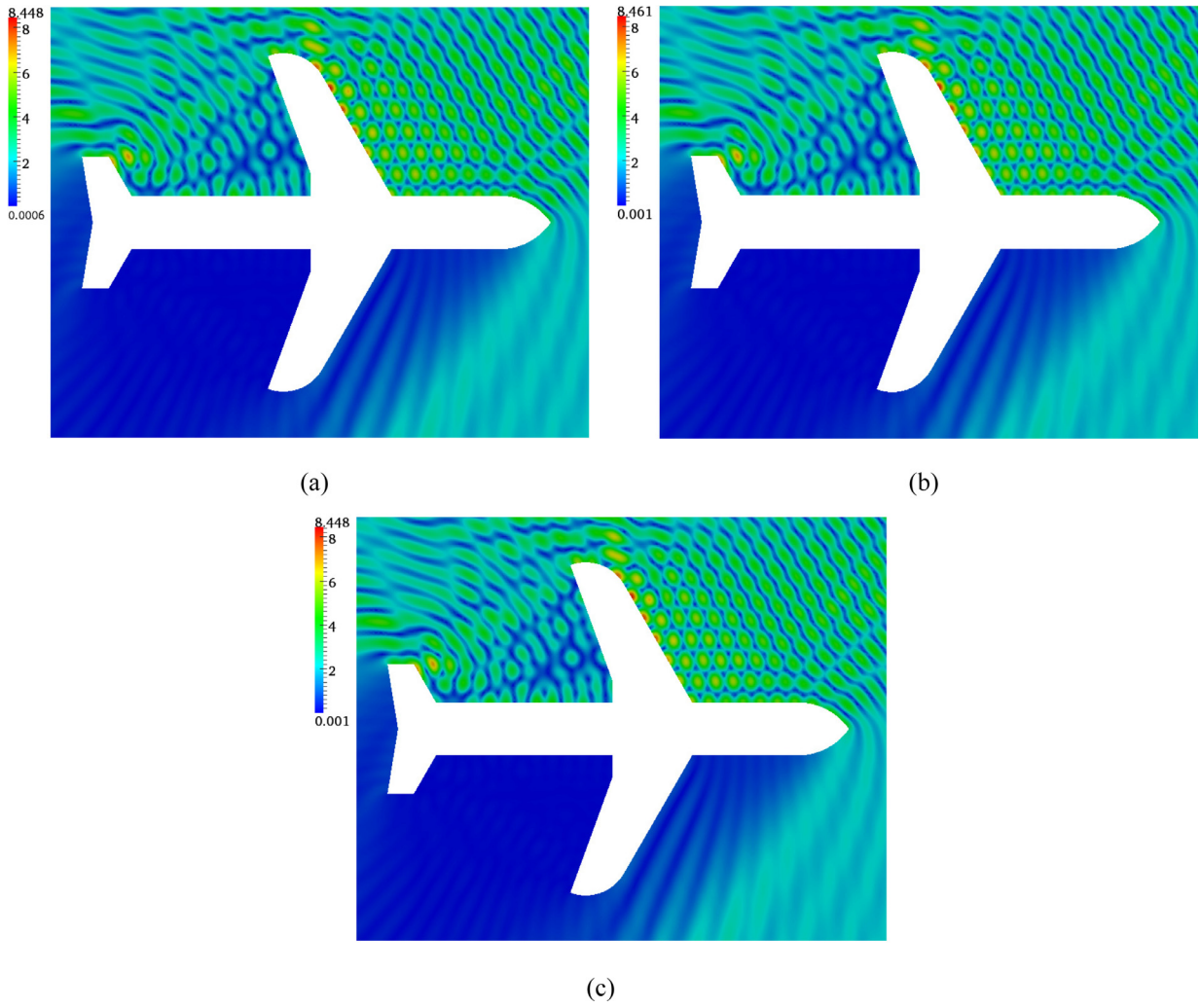

Fig. 21. Absolute value of total acoustic pressure of the airplane scattering problem for $k = 3$: (a) DiBFM-S1 with 1330 source nodes, (b) BFM-S1 with 1330 source nodes, and (c) BFM-S3 with 2652 source nodes.

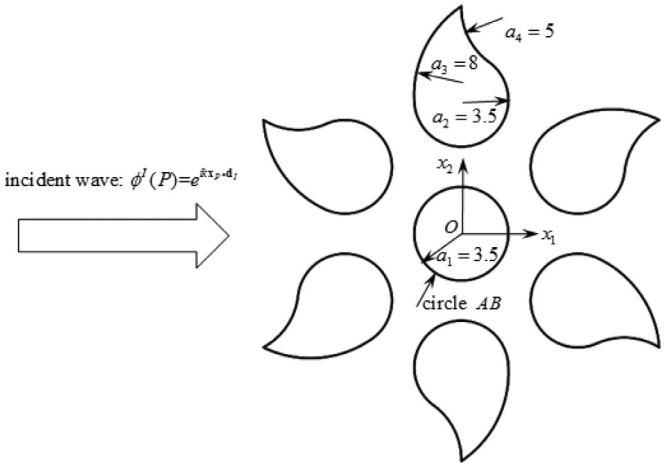

Fig. 22. Scattering from the multiple scatterers.

5. Numerical examples

In this section, four numerical examples are presented to demonstrate the accuracy and efficiency of the proposed method for solving 2D acoustic wave problems.

The relative errors are evaluated in a relative L_2-norm sense:

$$error = \frac{1}{|\phi|_{\max}}\sqrt{\frac{1}{M}\sum_{i=1}^{M}\left[\phi_i^{(e)} - \phi_i^{(n)}\right]^2}, \tag{16}$$

where $|\phi|_{\max}$ is the maximum absolute value of acoustic pressure φ_i over M sample points, $\phi_i^{(n)}$ and $\phi_i^{(e)}$ stand for the numerical and exact solutions, respectively.

In the following figures and tables, symbols '*Err_ϕ*', and '*Err_q*' represent the errors of acoustic pressure ϕ and its normal derivative $q = \frac{\partial\phi}{\partial n}$, respectively. The symbols 'DiBFM-S1' and 'DiBFM-S3' denote the numerical results of the DiBFM with S1 and S3 elements, respectively. The symbols 'BFM-S1' and 'BFM-S3' denote the numerical results of the BFM with conventional constant and quadratic elements, respectively. In addition, the symbol '*NS*' is the number of source nodes, and the symbol '*Time*' denotes the CPU time spent in constructing and solving the system equations.

5.1. Scattering from a rigid cylinder

In the first example, we consider a scattering problem on a rigid cylinder with radius $a = 1$ centred at the origin. As shown in Fig. 6, the cylinder is impinged by an plane wave $\phi^I(P)=e^{ik\mathbf{x}_P\cdot\mathbf{d}_I}$ propagating along the horizontal direction $\mathbf{d}_I = (1,\ 0)$. If point P inside domain, the analytical solution of the acoustic pressure can be calculated by the

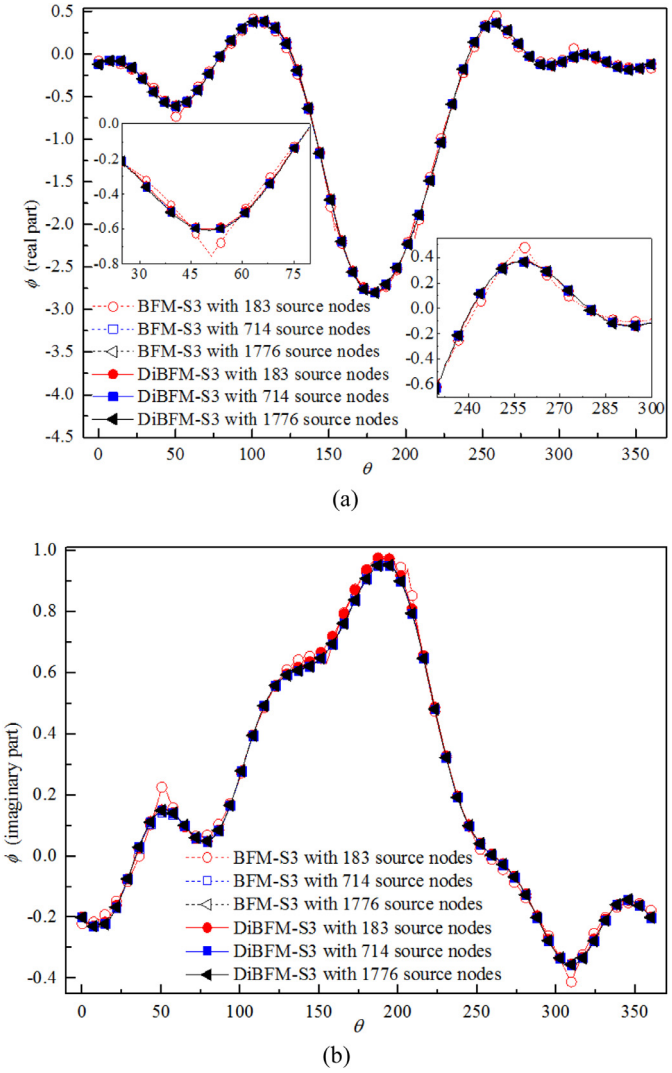

Fig. 23. Acoustic pressure along the circle *AB* of the multiple scatterers problem for $ka_1 = 3.5$: (a) real part and (b) imaginary part.

following infinite series:

$$\phi(P) = \phi^I(P) - \frac{\left[J_0^{(1)}(ka)\right]'}{\left[H_0^{(1)}(ka)\right]'} H_0(kr) - 2\sum_{n=1}^{\infty} i^n \frac{\left[J_n^{(1)}(ka)\right]'}{\left[H_n^{(1)}(ka)\right]'} H_n(kr)\cos(n\theta), \tag{17}$$

where $P = r(\cos\theta, \sin\theta)$ in polar coordinates, $J_n^{(1)}(\cdot)$ and $H_n^{(1)}(\cdot)$ are the first-kind of the Bessel function and Hankel function of order n, respectively. $[J_n^{(1)}(\cdot)]'$ and $[H_n^{(1)}(\cdot)]'$ denote the derivative of $J_n^{(1)}(\cdot)$ and $H_n^{(1)}(\cdot)$, respectively. If point P on the boundary of the cylinder, letting $r = a$ and hence Eq. (21) reduces to

$$\phi(P) = \frac{2}{\pi ka}\left\{\frac{i}{\left[H_0^{(1)}(ka)\right]'} + 2\sum_{n=1}^{\infty} \frac{i^{n+1}}{\left[H_n^{(1)}(ka)\right]'}\cos(n\theta)\right\}. \tag{18}$$

To demonstrate the accuracy and efficiency of the proposed method, a comparison between DiBFM and BFM is sought. Fig. 7 shows the accuracy of the two methods for solving the rigid cylinder scattering problem. For $ka = 5$ and $ka = 15$, external acoustic pressures ϕ along a semicircle *CD* are plotted in Figs. 8 and 9, respectively. For $ka = 10$ and $ka = 20$, acoustic pressures ϕ along the boundary *AB* are displayed in Figs. 10 and 11, respectively. Numerical results in Figs. 8–11 are obtained using 30, 60, 90 and 240 source nodes, respectively. Fig. 12 shows the CPU time spent in constructing and solving the system equations for the problem.

Table 1
Numerical results of the airplane scattering problem for $k = 3$.

DiBFM-S1		BFM-S1		BFM-S3	
NS	$\lvert\phi\rvert_{\max}$	*NS*	$\lvert\phi\rvert_{\max}$	*NS*	$\lvert\phi\rvert_{\max}$
332	8.355	332	8.383	324	8.803
1330	8.448	1330	8.461	1338	8.448
2664	8.448	2664	8.442	2652	8.448

From Figs. 7–12, DiBFM is able to obtain higher accuracy, convergence rates and computational efficiency than BFM. In particular, the S1 element in DiBFM (DiBFM-S1) can achieve the accuracy obtained by conventional quadratic boundary elements in BFM (BFM-S3). The reason for this is that the interpolation order of the dual interpolation elements is increased by two orders, in comparison with the interpolation order of the corresponding nonconforming elements. Besides, it is also concluded that the BFM is more sensitive to the mesh density than the DiBFM. For ka=5, the relative errors obtained by DiBFM-S3 is only 0.27% with 30 source nodes, while the relative errors shoot up to 3.86% obtained by the BFM-S3 with the same number of source nodes.

5.2. Radiation from a square

To demonstrate the accuracy of the proposed method near the corners, a radiation problem from a square is considered. The geometry and boundary conditions are shown in Fig. 13, and the analytical solution of the radiation problem is $\phi(x_1, x_2) = \frac{i}{4}H_0^{(1)}(kr)$, where $r = \sqrt{x_1^2 + x_2^2}$. To allow for comparison, this problem is also analyzed using BFM with an equivalent element refinement strategy.

In this example, the sample points closed to a corner *D* are evenly distributed over the line segments *DF* and *ED*. Fig. 14 compares the accuracy of the two methods near the corner *D*, for $k = 10$. Figs. 15 and 16 display the acoustic pressures ϕ and its derivatives $q = \frac{\partial\phi}{\partial n}$ along the segments *DF* and *ED*, respectively. From Figs. 14–16, it can be seen that the results in DiBFM are more accurate than those in BFM, especially for the points closed to corners. This study further demonstrates that the S1 element in DiBFM (DiBFM-S1) can achieve the accuracy obtained by conventional quadratic element (BFM-S3). In addition, the computational efficiency of the proposed method is higher than that of the conventional BFM (see Fig. 17).

5.3. Scattering from an airplane

To illustrate the ability of the proposed method to handle arbitrary geometries, a scattering problem from an airplane is analyzed. The principal dimension of the airplane is 31.9 m in length and 23.2 m in width. As shown in Fig. 18, the airplane is impinged by an plane wave $\phi^I(P) = 2e^{ik\mathbf{x}_P\cdot\mathbf{d}_I}$ propagating along the direction $\mathbf{d}_I = -(\sqrt{2}/2, \sqrt{2}/2)$, and the surface of the airplane is rigid. To allow for comparison, the problem is also solved using the BFM with conventional constant and quadratic boundary element.

Table 1 lists the maximum absolute values of the total acoustic pressure $|\phi|_{\max}$ for the two methods with different source nodes. Figs. 19 and 20 illustrate the real and imaginary parts of the acoustic pressure along the curve *AB*, respectively. Fig. 21 shows the contour plots of the absolute values of the total acoustic pressure $|\phi|$. From Table 1 and Figs. 19–21, it can be seen that the DiBFM using S1 elements (DiBFM-S1) provides a considerably higher fidelity solution than the BFM using conventional constant element (BFM-S1). Moreover, the numerical result of our method using S1 elements (DiBFM-S1) is almost consistent with that of the BFM using conventional quadratic element (BFM-S3).

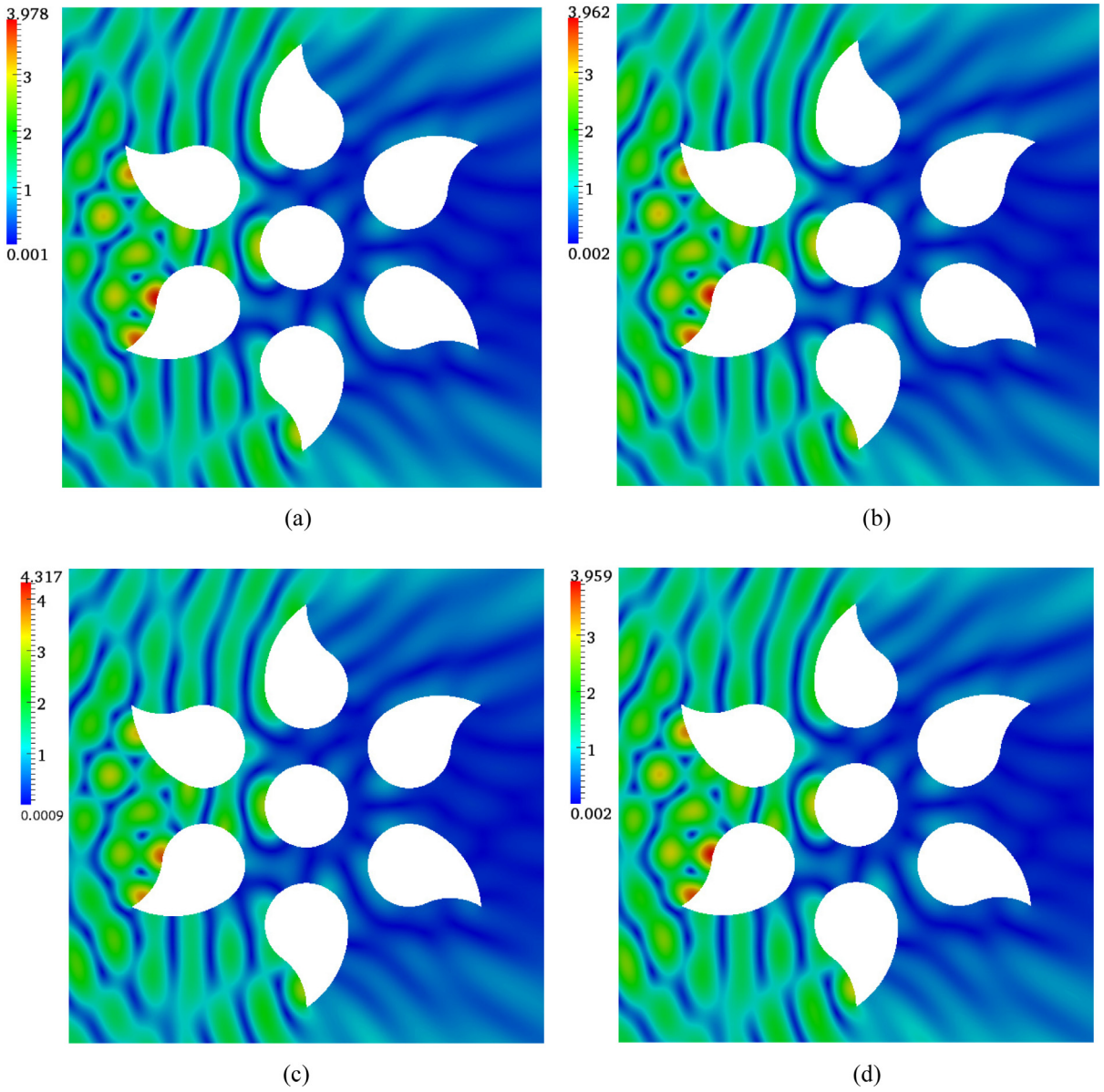

Fig. 24. Absolute value of total acoustic pressure of the multiple scatterers problem for $ka_1 = 3.5$: (a) DiBFM-S3 with 183 source nodes, (b) DiBFM-S3 with 1776 source nodes, and (c) BFM-S3 with 183 source nodes, and (d) BFM-S3 with 1776 source nodes.

This study further demonstrates the ability of the S1 element in DiBFM to achieve the accuracy comparable to that obtained by the conventional quadratic element.

5.4. Scattering from multiple scatterers

The fourth example is presented to show the ability of DiBFM for analyzing the multiple scatterers problem with internal reflections. As shown in Fig. 22, the multiple scatterers is impinged by an plane wave $\phi^I(P)=e^{ik\mathbf{x}_P\cdot\mathbf{d}_I}$ propagating along the direction $\mathbf{d}_I = (1,\ 0)$, and the surface of the multiple scatterers is rigid. In this example, the results using BFM with conventional quadratic elements are used for comparison.

The simulation results of the multiple scatterers problem are summarized in Table 2. The real and imaginary parts of the acoustic pressure along the circle *AB* are plotted in Fig. 23, respectively. The contour plots of the absolute values of the total acoustic pressure $|\phi|$ are shown in Fig. 24. It can be seen that the proposed method has higher accuracy and convergence rates than conventional BFM, confirming the conclusions drawn from the first three examples.

Table 2
Numerical results of the multiple scatterers problem for $ka_1 = 3.5$.

DiBFM-S3		BFM-S3	
NS	$\|\phi\|_{\max}$	*NS*	$\|\phi\|_{\max}$
183	3.978	183	4.317
348	3.956	348	3.934
714	3.962	714	3.952
1428	3.962	1428	3.958
1776	3.962	1776	3.959

This example illustrates an attractive feature: our method has the potential to seamlessly interact with CAD software. The feature derives from the fact that the geometric information of the computational model in the proposed method is highly consistent with the B-rep data structure of the geometric model in CAD software.

6. Conclusions and discussions

The DiBFM based on the Burton–Miller formulation has been proposed for solving 2D exterior acoustic wave problems. In our implementation, acoustic pressure and its derivative are approximated using the conforming elements, in the same way as conforming BFM. But the Burton–Miller integral equations are collocated at source nodes only, in the same way as nonconforming BFM. Thus, our method is able to unify the conforming and nonconforming elements in BFM implementation.

All presented numerical examples, with acoustic radiation or scattering problems, have demonstrated that the DiBFM can obtain higher accuracy, convergence rates and computational efficiency, in comparison with the conventional BFM. In particular, the S1 element in DiBFM is able to achieve the accuracy obtained by conventional quadratic boundary elements in BFM.

Extensions of our method to solve three-dimensional (3D) problems will substantially alleviate the task of the mesh generation. This is an attractive advantage of the proposed method. The reasons for this are as follows: (i) no geometric errors are introduced even in a coarse mesh; (ii) discontinuous grids are much easier to generate than continuous grids; and (iii) both continuous and discontinuous fields can be readily and accurately approximated using the proposed method, even if using discontinuous grids. This is an ongoing work.

Acknowledgements

This work was supported by National Natural Science Foundation of China under grant number 11772125.

References

[1] Wang XH, Zhang JM, Zhou FL. An adaptive fast multipole boundary face method with higher order elements for acoustic problems in three-dimension. Eng Anal Bound Elem 2013;37:114–52.
[2] Peake MJ, Trevelyan J, Coates G. The equal spacing of n points on a sphere with application to partition-of-unity wave diffraction problems. Eng Anal Bound Elem 2014;40:114–22.
[3] Chen LL, Chen HB, Zheng CJ. Structural–acoustic sensitivity analysis of radiated sound power using a finite element/discontinuous fast multipole boundary element scheme. Int J Numer Methods Fluids 2016;82(12):858–78.
[4] Sladek V, Sladek J, Tanaka M. Eigenvalue analysis of three-dimensional Helmholtz equation. Eng Anal Bound Elem 1993;11(2):165–70.
[5] Zheng CJ, Chen HB, Gao HF, Du L. Is the Burton–Miller formulation really free of fictitious eigenfrequencies? Eng Anal Bound Elem 2015;59:43–51.
[6] Zheng CJ, Gao HF, Du L, Zhang CZ. An accurate and efficient acoustic eigensolver based on a fast multipole BEM and a contour integral method. J Comput Phys 2016;305:677–99.
[7] Perrey-Debain E, Laghrouche O, Bettess P. Plane-wave basis finite elements and boundary elements for three-dimensional wave scattering. Philos Trans R Soc Lond A 2004;362(1816):561–77.
[8] Zhang JM, Qin XY, Han X. A boundary face method for potential problems in three dimensions. Int J Numer Methods Eng 2009;80:320–37.
[9] Qin XY, Zhang JM, Li GY. An element implementation of the boundary face method for 3D potential problems. Eng Anal Bound Elem 2010;34:934–43.
[10] Shu XM, Zhang JM, Han L, Dong YQ. A surface-to-surface scheme for 3D contact problems by boundary face method. Eng Anal Bound Elem 2016;70:23–30.
[11] Xie GZ, Zhang JM, Cheng H. A direct traction boundary integral equation method for three-dimension crack problems in infinite and finite domains. Comput Mech 2014;53(4):575–86.
[12] Banaugh RP, Goldsmith W. Diffraction of steady acoustic waves by surfaces of arbitrary shape. J Acoust Soc Am 1963;35:1590–601.
[13] Copley LG. Fundamental results concerning integral representations in acoustic radiation. J Acoust Soc Am 1963;44:28–32.
[14] Schenck HA. Improved integral formulation for acoustic radiation problems. J Acoust Soc Am 1968;44:41–58.
[15] Wu TW, Seybert AF. A weighted residual formulation for the chief method in acoustics. J Acoust Soc Am 1991;90:1608–14.
[16] Juhl P. A numerical study of the coefficient matrix of the boundary element method near characteristic frequencies. J Sound Vib 1994;175(1):39–50.
[17] Chen JT, Lin JH, Kuo SR. Boundary element analysis for the Helmholtz eigenvalue problems with a multiply connected domain. Proc R Soc Lond. Ser A 2001;457(2014):2521–46.
[18] Burton AJ, Miller GF. The application of integral equation methods to the numerical solution of some exterior boundary-value problems. Proc R Soc Lond Ser A 1971;323:201–10.
[19] Ma H, Kamiya N. Approximate formulation of the hypersingular boundary integral equation in potential theory. Eng Anal Bound Elem 2004;28:945–53.
[20] Mukherjee S. CPV and hfp integrals and their applications in the boundary element method. Int J Solids Struct 2000;37:6623–34.
[21] Liu YJ, Rizzo F. A weakly singular form of the hypersingular boundary integral equation applied to 3-D acoustic wave problems. Comput Methods Appl Mech Eng 1992;96(2):271–87.
[22] Guiggiani M, Krishnasamy G, Rudolphi T, Rizzo F. A general algorithm for the numerical solution of hypersingular boundary integral equations. ASME J Appl Mech 1992;59(3):604–14.
[23] Gao XW. An effective method for numerical evaluation of general 2D and 3D high order singular boundary integrals. Comput Methods Appl Mech Eng 2010;199:2856–64.
[24] Floreza WF, Powera H. Comparison between continuous and discontinuous boundary elements in the multidomain dual reciprocity method for the solution of the two-dimensional Navier–Stokes equations. Eng Anal Bound Elem 2001;25:57–69.
[25] Manolis GD, Banerjee PK. Conforming versus non-conforming boundary elements in three-dimensional elastostatics. Int J Numer Methods Eng 1986;23:1885–904.
[26] Parreira P. On the accuracy of continuous and discontinuous boundary elements. Eng Anal 1988;5(4):205–21.
[27] Zhang JM, Lin WC, Dong YQ. A dual interpolation boundary face method for elasticity problems. Eur J Mech 2019;73:500–11.
[28] Zhang JM, Lin WC, Dong YQ. A double-layer interpolation method for implementation of BEM analysis of problems in potential theory. Appl Math Model 2017;51:250–69.
[29] Zhang JM, Han L, Lin WC. A new implementation of bem by an expanding element interpolation method. Eng Anal Bound Elem 2017;78:1–7.
[30] Zhang JM, Zhong YD, Dong YQ. Expanding element interpolation method for analysis of thin-walled structures. Eng Anal Bound Elem 2018;86:82–8.
[31] Lancaster P, Salkauskas K. Surface generated by moving least squares methods. Math Comput 1981;37:141–58.